Electrochimica Acta 251 (2017) 588–594

Contents lists available at ScienceDirect

Electrochimica Acta

journal homepage: www.elsevier.com/locate/electacta

PdRu alloy nanoparticles of solid solution in atomic scale: outperformance towards formic acid electro-oxidation in acidic medium

Kanghua Miao[a], Yun Luo[b], Jiasui Zou[b], Jun Yang[b], Fengqi Zhang[b], Lin Huang[b], Jie Huang[a,*], Xiongwu Kang[b,*], Shaowei Chen[b,c]

[a] Department of Chemical Engineering, Shaanxi Key Laboratory of Physico-Inorganic Chemistry, Northwest University, Xi0an, Shaanxi 710069, China
[b] New Energy Research Institute, School of Environment and Energy, South China University of Technology, Guangzhou Higher Education Mega Centre, Guangzhou 510006, China
[c] Department of Chemistry and Biochemistry, University of California, 1156 High Street, Santa Cruz, California 95064, United States

ARTICLE INFO

Article history:
Received 10 July 2017
Received in revised form 28 July 2017
Accepted 28 August 2017
Available online 31 August 2017

Keywords:
PdRu alloy nanoparticles
solid solution
formic acid oxidation
electrocatalysis
stacking fault

ABSTRACT

Developing catalyst of high performance and low cost toward the electro-oxidation of formic acid on the anode of fuel cell is critical for the commercialization of direct formic acid fuel cells. Here we reported the synthesis of Pd_xRu_{10-x} (x = 1,3,5,7,9) nanoparticles (NPs) by concurrent reduction of Pd^{2+} and Ru^{2+} in polyol solution at 200 °C. The particle size of the obtained NPs was confined at 5–15 nm in diameter. X-ray diffraction (XRD) analysis revealed face-centered cubic (fcc) crystal structure for Pd_xRu_{10-x} (x = 3,5,7,9), with the lattice parameter proportional to the Pd content. The formation of the solid solution in atomic scale was confirmed for the alloy nanoparticles by XRD and the elemental mapping. Williamson-Hall method revealed that the stacking fault was dependent on the alloying extent of the alloy nanoparticles and reached the minimum for Pd_5Ru_5, which exhibited the highest activity towards formic acid oxidation among all these prepared samples, with mass activity of 12.6 times higher than that of commercial Pd/C. It was observed that the highest catalytic activity was in agreement with the minimum of the stacking fault of the alloy nanoparticles.

1. Introduction

Direct formic acid fuel cells (DFAFCs) based on proton exchange membrane have received growing attention [1–5] due to higher open circuit voltage (1.450 V) than direct methanol fuel cell (1.190 V) or H_2 fuel cell (1.229 V) [6], low crossover rate through the Nafion membrane [4], more energy per volume of fuel carried than methanol [1,7,8]. In addition, conventional catalysts for fuels oxidation, for example, H_2, methanol or ethanol oxidation, are mainly based on Pt [9–11]. Considering the abundance of Pt in earth crust, the large-scale commercialization of fuels cells based on such fuels might be limited because of the high price of the catalysts. Pd based nanomaterials, more abundant than Pt in earth crust and thus more cost-effective, have been reported more active towards formic acid oxidation reaction (FAOR) with respect to Pt counterparts [12,13], rendering Pd based anodes more affordable. To further improve the catalytic activity of Pd based catalysts, many efforts have been devoted to modify the size, morphology and composition of Pd NPs. For example, Zhou et al. studied the size effect of the pure Pd nanoparticles and observed a volcano shape curve for the electro-activity over the size of the Pd NPs. The highest activity could be found on NPs with diameter of 5–7 nm, which was attributed to the geometric effect [14,15]. Alloying with a second metal, Fe [16], Co [17], Ni [18], Cu [19], Au [20,21], Ag [22], and Pt [23,24], was equally found to be an effective pathway to improve the catalytic activity of Pd catalysts.

Ru, as an efficient catalyst itself [25,26], remarkably improved the catalytic performance via alloying with Pt [27,28], is expected to equally enhance the catalytic activity by alloying with Pd and outperform any other metals. Cao et al. reported the synthesis of Pd_xRu_{100-x}(x = 20, 40, 60, 75, 90) alloy nanoparticles of 3–5 nm by one-pot polyol reduction procedure and observed that $Pd_{60}Ru_{40}$ exhibited that best mass activity out of Pd_xRu_{100-x}(x = 20, 40, 75, 90) [29,30] which is 4.1-fold higher than Pd/C or pure Pd nanoparticles under the same condition. However, it is hard to

* Corresponding authors.
E-mail addresses: huangjie@nwu.edu.cn (J. Huang), esxkang@scut.edu.cn (X. Kang).

http://dx.doi.org/10.1016/j.electacta.2017.08.167
0013-4686/

Table 1
Preparation condition for Pd_xRu_{10-x} (x = 1, 3, 5, 7, 9) nanoparticles.

Sample	$Na_2[PdCl_4]$ (mg)	$RuCl_3$ (mg)	TEG (mL)	PVP (mmol)
Pd_1Ru_9	29.4	235.6	100	1
Pd_3Ru_7	88.3	180.3	100	1
Pd_5Ru_5	147.3	131.1	100	1
Pd_7Ru_3	206.1	62.4	100	1
Pd_9Ru_1	264.8	25.9	100	1

know if Pd_xRu_{100-x} solid solution formed in atomic scale, since no detailed and solid data, such as X-ray diffraction (XRD) analysis, was provided. Kusada and coworkers [31] synthesized Pd_xRu_{10-x}(x = 1, 3, 5, 7, 9) with the size of 10 nm and confirmed the formation of the solid solution in atomic scale by both XRD and elemental mapping in transmission electron microscopy (TEM), demonstrating excellent CO oxidation activity. Since alloying with a second metal may lead to third body effect, close and proximal contact of Ru and Pd in solid soluiton in atomic ratio of 1:1 might maximize the third body effect and the number of active sites on nanoparticles surface [32] and thus Pd_5Ru_5 might exhibit excellent electrocatalytic activity toward formic acid oxidation. This is primary purpose of the current study.

Herein, by following Kusada's method [31], we synthesized well-dispersed Pd_xRu_{10-x} (x = 1-9) alloy NPs of solid solution in atomic scale, as confirmed by XRD and elemental mapping and characterized the electro-catalytic activity toward formic acid oxidation. It was found that the as-synthesized Pd_5Ru_5 alloy NPs exhibited 12.6-folds higher mass activity with respect to commercial Pd/C catalysts, outperformed these PdRu alloy nanoparticles reported so far. In addition, the mechanism behind the enhancement of catalytic activity of Pd_xRu_{1-x} nanoalloys were discussed in terms of electronic modification of Ru on Pd and the microstructure effect, e.g. stacking fault.

2. Experimental

2.1. Chemicals

Ruthenium chloride ($RuCl_3$, 99%, ACROS), poly(N-vinyl-2-pyrrolidone) (PVP, MW ≈ 40000, Energy Chemical), carbon black (Vulcan XC-72, Cabot), triethylene glycol (TEG, MACKLIN), disodium tetrachloropalladate ($Na_2[PdCl_4]$, 99%, Energy Chemical), nafion(0.5 wt%, Alfa Aesar), Pd/C(20 wt%, Alfa Aesar), ethanol absolute(DM) and acetone(DM). All chemicals were used as received from commercial suppliers without further treatment. Ultra-pure water obtained from a Barnstead Nanopure water system (18.2 MΩ cm) was used in this work.

2.2. Synthesis of Pd_xRu_{10-x} (x = 1, 3, 5, 7, 9) nanoparticles

In a typical synthesis [31] of Pd_5Ru_5 nanoparticles, 444 mg of PVP was dissolved in 100 mL of TEG and the solution was heated to 200 °C in oil-bath with magnetic stirring. Meanwhile, 147.3 mg of $Na_2[PdCl_4]$ and 131.1 mg of $RuCl_3$ were dissolved in 40 mL of water.

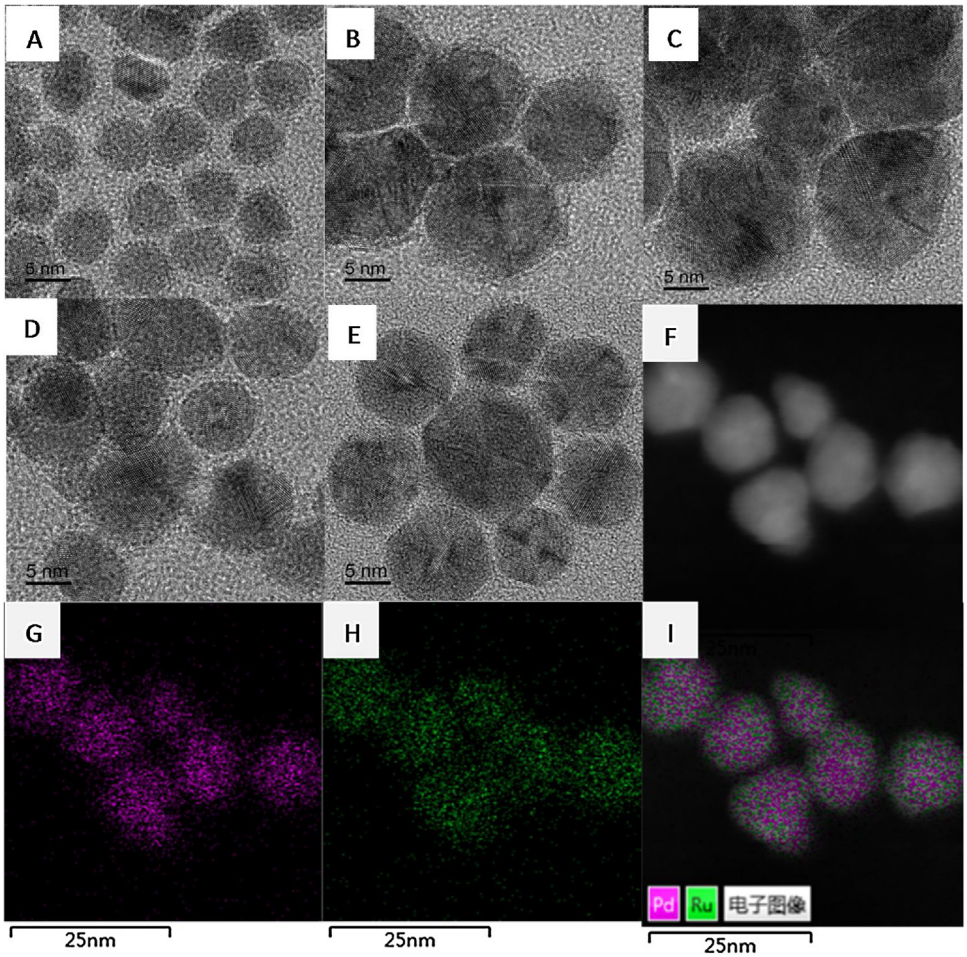

Fig. 1. The TEM images of (A) Pd_1Ru_9, (d = 5.90 ± 0.51) (B) Pd_3Ru_7(14.6 ± 1.6),(C) Pd_5Ru_5(15.7 ± 1.1), (D) Pd_7Ru_3(d = 8.5 ± 0.9), and (E) Pd_9Ru_1(d = 10.7 ± 1.2) nanoparticles. (F) HAADF-STEM image, (G) Pd-L and (H) Ru-L and (I) overlap of both Pd-L and Ru-L STEM−EDX mapping obtained for Pd_5Ru_5 nanoparticles.

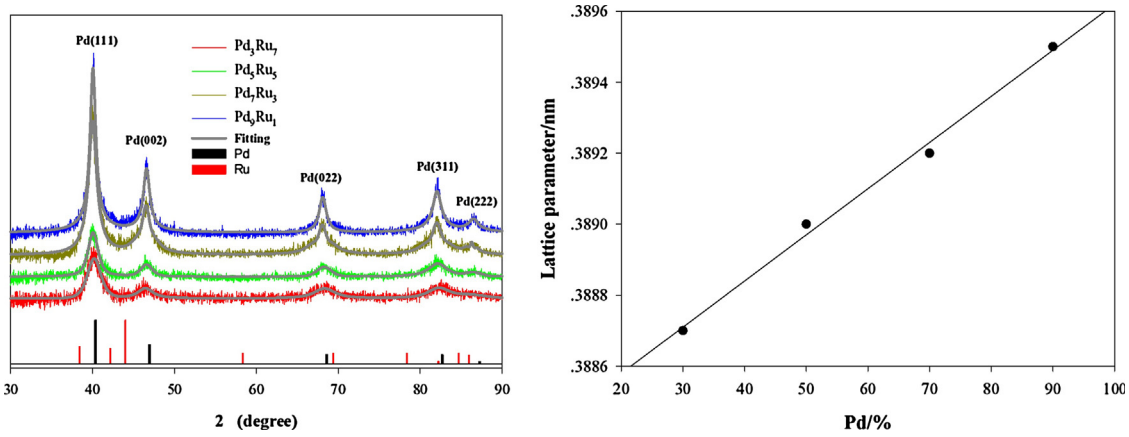

Fig. 2. (A) The XRD patterns of Pd_xRu_{10-x} (x = 3,5,7,9) nanoparticles, with both raw data (colored lines) and fitted results from Fityk software (grey solid lines) and (B) dependence of the lattice parameter on the content of Pd in the alloy nanoparticles.

Such a solution was then slowly added into the TEG at 200 °C. After cooling to room temperature, acetone and alcohol were added to precipitate nanoparticles, followed by centrifugation. This step was repeated 5 times to remove unbound PVP from the particles surface. Other Pd_xRu_{10-x} (x = 1, 3, 7, and 9) samples were prepared via the same protocol, by controlling the molar ratio of Pd^{2+} to Ru^{3+} as summarized in Table 1.

2.3. Characterization

The powder X-ray diffraction (pXRD) measurements were carried out by a Bruker D8 diffractometer with Cu Kα radiation (λ = 0.15406 nm). The elemental compositions and valence states of Pd_xRu_{10-x} alloy nanoparticles were examined by X-ray photoelectron spectroscopy (XPS, Phi X-tool instrument). HRTEM images of the nanoparticles were acquired on JEOL TEM-2010 for the analysis of the size distribution.

2.4. Electrochemical measurements

The catalyst ink was prepared by first dispersing carbon black (Vulcan XC-72) in ethanol upon sonication for 1 h and then the as-prepared Pd_xRu_{10-x} NPs for another 2 h, with the mass ratio of nanoparticles to carbon black 20: 80. Prior to the catalyst deposition, the glassy carbon electrode (GCE,Φ=6 mm) was subjected to mechanical polishing with 0.3 μm alumina powders on a polishing microcloth for 20 min, successively sonicated in ultra-pure water and sulfuric acid solution (3 M) for 10 min. It was then cleaned under UV irradiation for 10 min to remove the organics on the surface. The cleaned GCE was coated by 10 μg catalyst ink (1 mg/ml), dried under air flux in room temperature. Then 5 μL of Nafion (0.5 wt%) was deposited on top of the nanoparticles and dried in air. The electrochemical chacterizations were carried out on a CHI 650E electrochemical workstation (CH Instruments Inc.), with a conventional three-electrode system at room temperature (25 °C). The GCE prepared above was used as the working electrode, a Hg/Hg_2Cl_2 with saturated KCl solution as the reference electrode and a Pt slice as counter electrode. The cyclic voltammetric measurements were performed at the scan rate of 100 mV s^{-1} in 0.5 M perchloric acid, from which the electrochemical surface area (ECSA) was determined from the hydrogen underpotential depostion (H_{upd}) region [14]. The electro activity toward formic acid oxidation and stability test were carried out in 0.5 M formic acid in 0.5 M perchloric acid solution at the scan rate of 50 mV s^{-1}. The CO stripping was investigated in 0.5 M perchloric acid solution at the scan rate of 5 mV s^{-1}. First, the 0.5 M perchloric acid solution was purged with N_2 for 20 min. Then chronoamperometric measurement was initiated at 0.2 V (vs SCE) with CO bubbling for 5 min. Upon chronoamperometric measurement and CO bubbling stopped, the solution was purged again by N_2 for 20 min, followed by 2 cycles of CV measurement with scan rate of 5 mV/s.

Table 2
Parameters evaluated from XRD patterns: crystallite size (L_v/nm), stacking fault (α/%) and micro-strain effect (ε/%).

Sample	L_v	α	ε
Pd_3Ru_7	10.5	0.79	1.15
Pd_5Ru_5	10.2	0.07	0.69
Pd_7Ru_3	10.5	0.79	0.25
Pd_9Ru_1	11.5	0.85	0.011

3. Results and discussion

HRTEM images of as-prepared Pd_xRu_{10-x} (x = 1, 3, 5, 7, 9) nanoparticles are shown in Fig. 1. The mean diameters of the nanoparticles were determined to be (A) 5.90 ± 0.51, (B) 14.55 ± 1.57, (C) 15.69 ± 1.12, (D) 8.46 ± 0.92, and (E) 10.66 ± 1.16 nm for Pd_xRu_{10-x} (x = 1, 3, 5, 7, 9), respectively, in agreement with that reported in earlier publication [31]. TEM images of Pd_xRu_{10-x} (x = 1, 3, 5, 7, 9) nanoparticles in lower magnification scales and the size distribution histograms were displayed in Figs. S1–S5 and Fig. S6 respectively. The Pd_xRu_{10-x} (x = 1, 3, 5, 7, 9) nanoparticles were successfully mixed and loaded on carbon black. As shown in Fig. S3, Pd_5Ru_5 nanoparticles were well dispersed on carbon support. Fig. 1 (F) to (I) shows STEM image and elemental mapping data for Pd_5Ru_5 nanoparticles. It can be seen that both Pd and Ru elements homogeneously distribute all over a nanoparticle, supporting the formation of solid solution Pd_5Ru_5 alloy.

The crystal structures of Pd_xRu_{10-x} samples were investigated by XRD measurements, depicted in Fig. 2 (A). The standard XRD patterns for face centered cubic (fcc) structure of Pd (JCPDS no. 01-075-6724) and hexagonal closed packed (hcp) structure of Ru (JCPDS no. 01-089-4903) are used as references. It was clearly observed that well-defined fcc phase was observed all the samples except for Pd_1Ru_9 displaying more likely hcp phase. With the assistance of the free Fityk software [33], each diffraction peak for fcc phase were fitted via Pearson VII function and depicted in Fig. S7. The sum curve of the fitting peaks overlap very well with raw data (solid gray lines). In Fig. 2 (A), diffraction peaks for Pd_xRu_{10-x} (x = 3, 5, 7, 9) samples, correspond to (111), (002), (022),

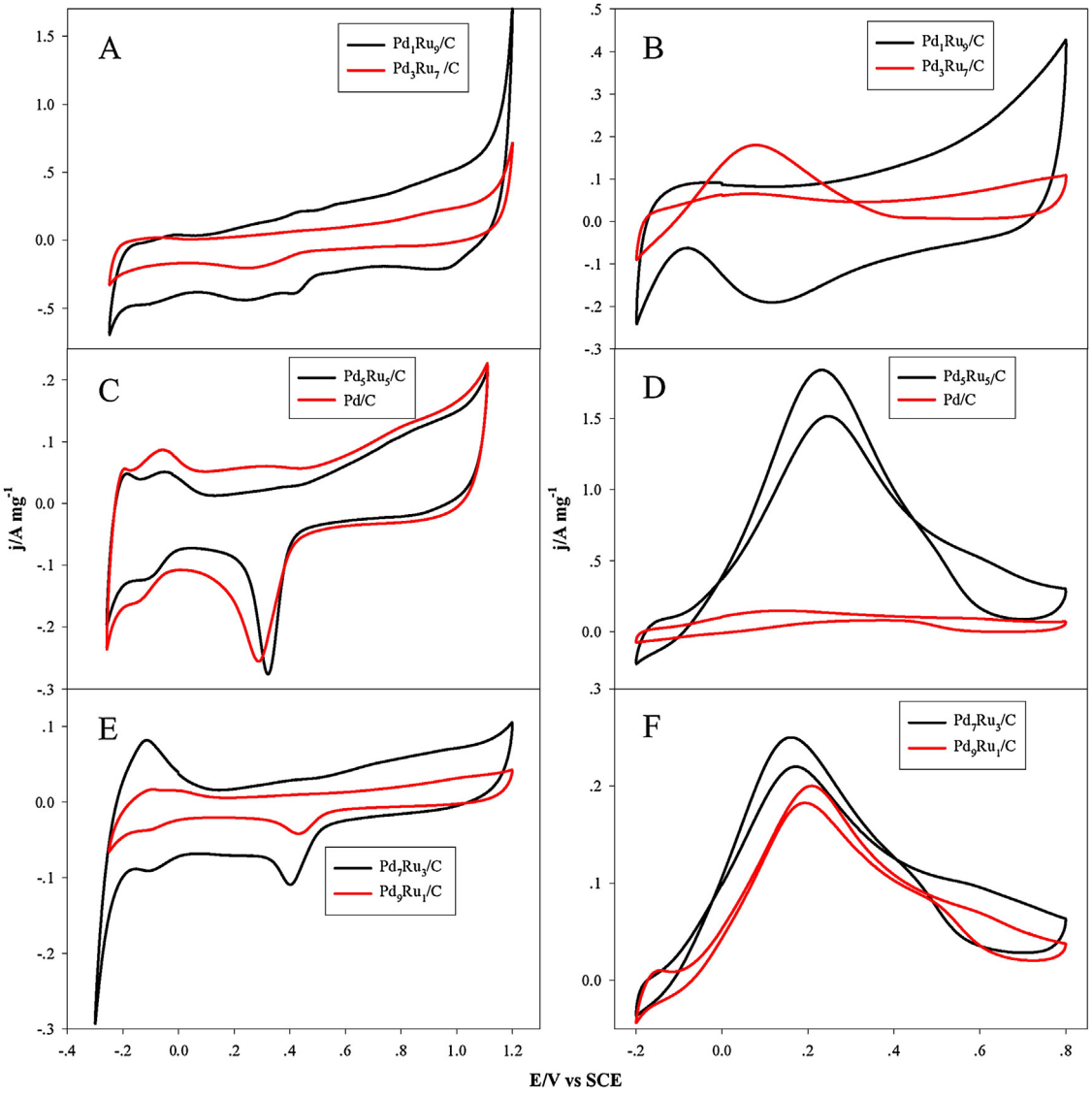

Fig. 3. Cyclic voltammograms of Pd_1Ru_9, Pd_3Ru_7, Pd_5Ru_9, Pd/C, Pd_7Ru_3 and Pd_9Ru_1 samples in 0.5 M $HClO_4$ with potential scan rate of 100 mV s^{-1} (A, C, E) and 0.5 M $HClO_4$ +0.5 M HCOOH with potential scan rate of 50 mV s^{-1}(B, D, F), with the currents normalized to the unit mass loading of Pd metal.

Table 3
The ESCA and j_{max} of all samples, derived from Fig. 3.

samples	Pd/C	Pd_1Ru_9/C	Pd_3Ru_7/C	Pd_5Ru_5/C	Pd_7Ru_3/C	Pd_9Ru_1/C
ESCA (m^2/g)	50.5	13.4	6.4	39.6	4.2	10.4
j_{max}(A/mg^{-1})	0.15	0.08	0.18	1.9	0.25	0.20

(311), (222) facets of Pd fcc phase respectively. Based on Bragg's law, the lattice parameter (a_{fcc}) of fcc structure were derived from 2θ. As depicted in Fig. 2 (B), the lattice parameter of the alloy nanoparticles was decreased linearly when Pd at% was decreased, indicating a trend of lattice contraction. These facts reveal the dissolution of Ru atoms into Pd lattice in Pd_xRu_{10-x} (x = 3, 5, 7, 9) samples. Taking STEM results in Fig. 1 into account, one can thus confirm the formation of PdRu alloy nanoparticles of solid solution in atomic scale for Pd_xRu_{10-x} (x = 3, 5, 7, 9) samples.

The microstructural information, such as micro-strain (ε), stacking fault (α) and crystallite size (L_ν) were estimated based on the Williamson-Hall method, following the calculation procedure in literatures [34,35], cf. Eq. (3)

$$\frac{\beta\cos\theta}{\lambda} = \frac{\kappa}{L_\nu} + \frac{K_{hkl}}{a_{fcc}}\alpha + \frac{4\sin\theta}{\lambda}\varepsilon \quad (3)$$

where β is the full-width at half-maximum (FWHM) of the diffraction peak, λ = 0.154056 nm, θ diffraction angle in radians, κ is the Scherrer constant considering equal to 1, K(111) = 0.43, K(200) = 1, K(220) = 0.71, K(311) = 0.45 and K(222) = 0.43. According to the results listed in Table 2, the L_ν value are similar for Pd_xRu_{10-x} (x = 3, 5, 7, 9) samples, lower than or close to mean particle diameters determined by TEM. The stacking fault for Pd_5Ru_5 was the lowest (0.07), Pd_9Ru_1 (0.85) the highest and Pd_3Ru_7 and Pd_7Ru_3 in the between. This is in agreement with earlier reports, [36,37]. that alloying with a second metal element decreased the stacking fault energy and thus unfavor the formation of stacking fault. Thus the dependence of the stacking fault on the alloying component might indicate the stacking fault in these alloy nanoparticles mainly originated from the partial dislocations, instead of planar vacancies as considered traditionally [38]. It was also noticed that the micro-strain increased steadily with the Ru content in the alloy

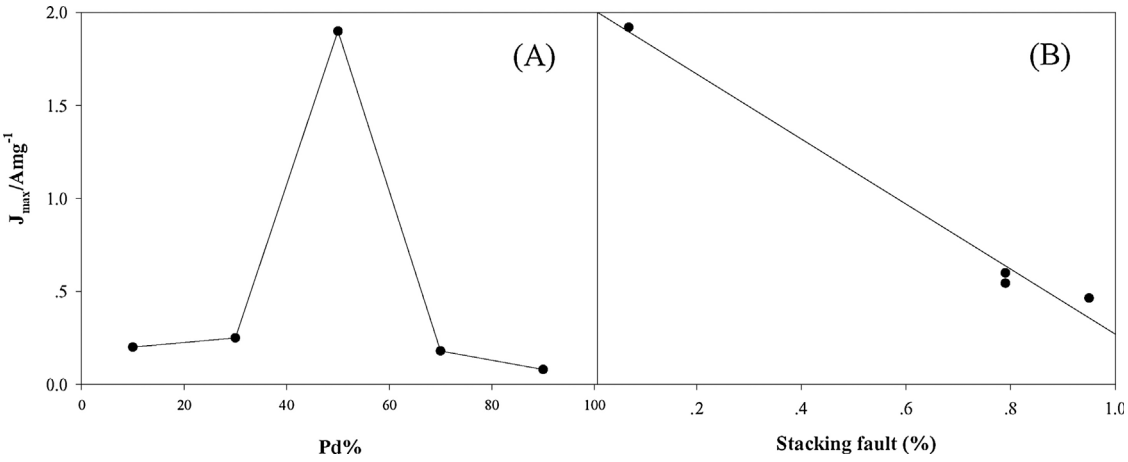

Fig. 4. Dependence of the mass activity on (A) the Pd content and (B) the stacking fault of the alloy nanoparticles Pd_xRu_{10-x} (x = 1, 3, 5, 7, 9).

nanoparticles, suggesting that the micro-strain was mainly contributed from the Ru component, probably because Ru is more difficult to be crystallized than Pd as observed in earlier report [29].

Fig. 3A, C, E showed the cyclic voltammograms of Pd_xRu_{10-x}/C and Pd/C in 0.5 M $HClO_4$ solution at a potential scan rate of 100 mV s^{-1} at room temperature. The currents have been normalized to the unit mass loadings of Pd. The current between −0.25 and 0.0 V can be ascribed to the adsorption/desorption of hydrogen and perchlorate on the Pd surfaces, as well as the absorption of a small fraction of hydrogen into the Pd lattice [39,40]. A well-defined cathodic peak at around +0.35 V can be observed due to the reduction of Pd oxide that was formed in the anodic scan. This provides a convenient method to determine the electrochemical surface area (ECSA) of Pd, without the complication of surface contamination, as occurred for other methods [41,42]. According to this method, the specific ECSA of the Pd_5Ru_5/C nanoparticles was estimated and listed in Table 3. The ESCA for Pd_5Ru_5/C was derived to be 39.6 m^2/g, 21.6% less than that of Pd/C (50.5 m^2/g).

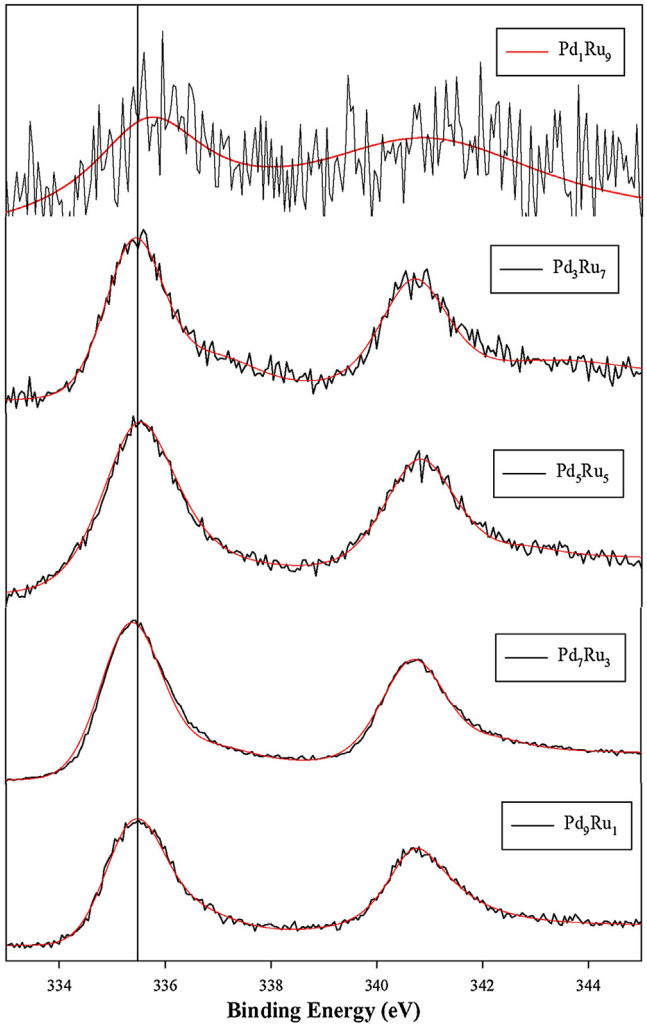

Fig. 5. XPS spectrum of Pd_xRu_{10-x} (x = 1, 3, 5, 7, 9) alloy NPs (Smoothed curves were plotted in red color for guide of eye).

Fig. 3B, D, F depicted the voltammograms of the Pd_xRu_{5x-x}/C and Pd/C catalysts recorded in a 0.5 M HCOOH + 0.5 M $HClO_4$ solution at a potential scan rate of 50 mV s^{-1} for evaluation of the electrocatalytic activity and the peak current density were listed in Table 3. It can be seen that the maximum current was achieved by Pd_5Ru_5/C nanoparticles, which is as high as 1.9A mg$^{-1}_{Pd}$, about 12.6 times higher than that of reference Pd/C (0.15 Amg$^{-1}_{Pd}$). Such an enhancement is superior to reported ones in literatures. Zhou et. al reported Pd nanoparticles capped by butylphenyl ligand and achieved mass activity of Pd nanoparticles that is 4.5 times that of Pd black [43]. Wu et. al synthesized sub 5 nm PdRu alloy nanoparticles and reached the mass activity of 4.1 times that of commercial Pd black.

By either decreasing or increasing the Pd content in Pd_xRu_{1-x} nanoparticles, both ECSA and formic acid catalytic activity were reduced significantly and thus the dependence of mass activity of Pd over Pd content demonstrated a volcano shape, as shown in Fig. 4(A). Although the size of Pd_3Ru_7 and Pd_5Ru_5 are quite similar to each other according to TEM and XRD analysis, the ECSA of Pd_5Ru_5 is almost 6 times that of Pd_3Ru_7. Although Pd_7Ru_3 and Pd_9Ru_1 nanoparticles have both higher Pd content and are smaller than Pd_5Ru_5 in diameter, but the ESCA of Pd_7Ru_3 and Pd_9Ru_1 are still much smaller than that of Pd_5Ru_5, in contrast to that observed for pure Pd nanoparticles [14]. Thereafter, it can be concluded that the high catalytic activity of Pd_5Ru_5/C resulted probably from both the larger ECSA and higher density of the catalytic active sites on the nanoparticles surface introduced by the alloying with the right ratio of two metals.

It has been reported that the catalytic activity toward the formic acid is very sensitive to that of crystallographic faces since the catalytic oxidation reaction require the right geometry for activating the formic acid adsorption. Fig. 4 (B) depicted the peak current density over the stacking fault of the alloy nanoparticles,

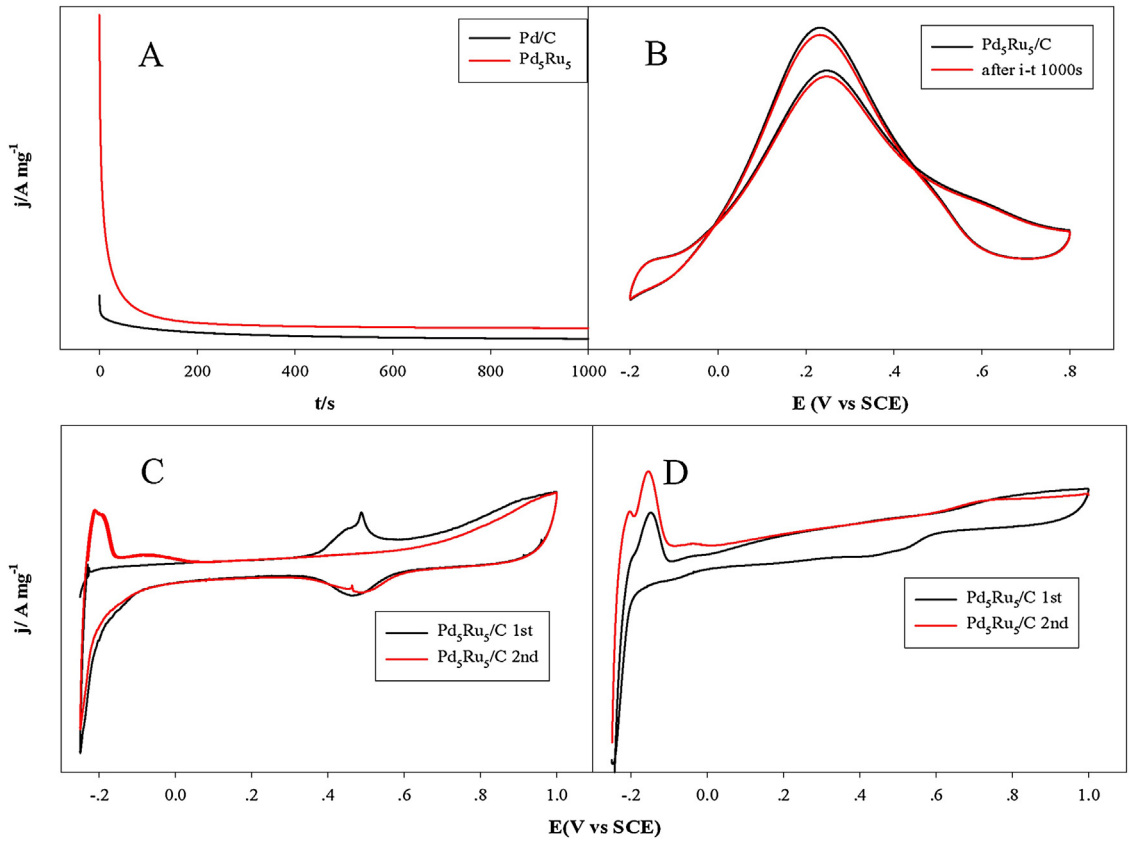

Fig. 6. (A) Chronoamperometric measurements for Pd/C (black) and Pd_5Ru_5/C (red) alloy nanoparticles; (B) CV of Pd_5Ru_5/C before (black) and after chronoamperometric measurement of 1000 s (red); (C) 1st and 2nd CV scans of Pd_5Ru_5/C in 0.5 M $HClO_4$, potential scan rate of 5 mV s^{-1} in the absence of CO after chronoamperometric measurement for 5 min in the presence of CO and (D)1st and 2nd CV scans of Pd_5Ru_5/C after chronoamperometric measurement of 1000 s in 0.5 M $HClO_4$ +0.5 M HCOOH, potential scan rate of 5 mV s^{-1}.

from which a linear dependence was observed, where the smallest stacking fault but highest catalytic activity was observed for Pd_5Ru_5 nanoparticles. It is highly possible that the stacking fault reflected the defects of the nanoparticles on the surface and thus the geometry of the Pd atoms (active sites) toward the oxidation of formic acid, thus partially account for activity of these alloy metal nanoparticles [15].

It has been reported that the d band center of Pd metal is another critical parameter that might dominate the catalytic activity of PdRu alloy nanoparticles [14,15]. For this purpose, the binding energy of Pd, a direct reflection of the d band center of Pd in RuPd alloy nanoparticles, were measured and depicted in Fig. 5. Unlike the significant change of 1.5 eV of the biding energy for Pd in Pd_xRu_{1-x} alloy nanoparticles in sub–5 nm sized nanoparticles [29], no apparent shift of the binding energy for Pd were observed for Pd_xRu_{1-x} alloy nanoparticles with the change of the composition of Pd except that for Pd_1Ru_9, suggesting that the d band center barely contributed to the outstanding catalytic activity of Pd_5Ru_5 in relative to other alloy nanoparticles Pd_xRu_{1-x} (x = 3, 7, 9).

Fig. 6 (A) shows the chronoamperometric profiles of Pd/C (black) and Pd_5Ru_5/C (red) with the potential set at 0.2 V for 1000 s. The initial high currents, caused by the combination of formic acid oxidation and double-layer charging, quickly decayed and reached steady state probably due to the adsorption of poisoning intermediates [44,45]. CV scans before and after chronoamperometric measurement of 1000 s were almost identical to each other, as depicted in Fig. 6 (B), indicating that the activity of the catalyst was able to be recovered after chronoamperometric measurement and the catalyst itself was stable. In other words, the decay of the current in chronoamperometric measurement resulted from the poisoning intermediates of the formic acid oxidation, instead of the degradation of the catalyst itself. To verify if the attenuation of catalyst activity was due to the CO_{ads} poisoning [46], we conducted two CV scans after chronoamperometric measurements in the presence and absence of CO in formic acid solution respectively, as shown in Fig. 6 (C) and (D). In Fig. 6 (C), the first scan displayed at anodic peak at 0.5 V due to the oxidation of CO_{ads}, meanwhile no H deposition features were observed from −0.2 to 0.0 V, due to the active surface were covered by CO_{ads}. In the second scan, the anodic peak at 0.5 V vanished and the H deposition features were recovered, due to the removal of CO_{ads} in the first CV scan. In contrast, no such features were observed for Pd_5Ru_5/C samples after chronoamperometric measurement for formic acid oxidation, as shown in Fig. 6 (D), suggesting that the current attenuation in chronoamperometric measurement in Fig. 6(A) was not caused by carbon monoxide poisoning, but some other unknown organic intermediates during formic acid oxidation reaction [6].

4. Conclusions

Alloy nanoparticles of solid solution Pd_xRu_{10-x} (x = 1, 3, 5, 7, 9) were prepared by following the reported procedure. The structure of the prepared samples was characterized by XRD analysis and elemental mapping, confirming the formation of alloy in atomic scale. The electro-catalytic activity of the alloy nanoparticles toward formic acid oxidation was tested and the highest activity was achieved by Pd_5Ru_5/C, which is 12.5 times higher than that of Pd/C. A volcano shape dependence of the activity of these alloy nanoparticles on the composition of alloy nanoparticles was observed, which was further found to be linearly dependent on the

stacking fault of the alloy nanoparticles estimated by the Williamson-Hall method.

Acknowledgments

This work was supported by the National Natural Science Foundation of China (No. 51602106) and Technology Research and Development Program of Shanxi Province, China (No.14JF025).

Appendix A. Supplementary data

Supplementary data associated with this article can be found, in the online version, at http://dx.doi.org/10.1016/j.electacta.2017.08.167.

References

[1] C. Rice, S. Ha, R.I. Masel, A. Wieckowski, Catalysts for direct formic acid fuel cells, Journal of Power Sources 115 (2003) 229–235.
[2] H. Su, C.A. Rice, R.I. Masel, A. Wieckowski, Methanol conditioning for improved performance of formic acid fuel cells, Journal of Power Sources 112 (2002) 655–659.
[3] R.H. Tammam, M.M. Saleh, Electrocatalytic oxidation of formic acid on nano/micro fibers of poly(p-anisdine) modified platinum electrode, Journal of Power Sources 246 (2014) 178–183.
[4] Y.W. Rhee, Y.H. Su, R.I. Masel, Crossover of formic acid through Nafion((R)) membranes, Journal of Power Sources 117 (2003) 35–38.
[5] L. Zhang, Y. Tang, J. Bao, T. Lu, C. Li, A carbon-supported Pd-P catalyst as the anodic catalyst in a direct formic acid fuel cell, Journal of Power Sources 162 (2006) 177–179.
[6] X.W. Yu, P.G. Pickup, Recent advances in direct formic acid fuel cells (DFAFC), Journal of Power Sources 182 (2008) 124–132.
[7] O. Winjobi, Z.Y. Zhang, C.H. Liang, W.Z. Li, Carbon nanotube supported platinum-palladium nanoparticles for formic acid oxidation, Electrochimica Acta 55 (2010) 4217–4221.
[8] S. Uhm, H.J. Lee, Y. Kwon, J. Lee, A Stable and Cost-Effective Anode Catalyst Structure for Formic Acid Fuel Cells, Angewandte Chemie 120 (2008) 10317–10320.
[9] S.M. Mitrovski, L.C. Elliott, R.G. Nuzzo, Microfluidic devices for energy conversion: Planar integration and performance of a passive fully immersed H2- O2 fuel cell, Langmuir 20 (2004) 6974–6976.
[10] M. Ruan, X. Sun, Y. Zhang, W. Xu, Regeneration and Enhanced Catalytic Activity of Pt/C Electrocatalysts, Acs Catal 5 (2015) 233–240.
[11] F. Saleem, Z. Zhang, B. Xu, X. Xu, P. He, X. Wang, Ultrathin Pt-Cu nanosheets and nanocones, Journal of the American Chemical Society 135 (2013) 18304.
[12] C. Rice, S. Ha, R.I. Masel, P. Waszczuk, A. Wieckowski, T. Barnard, Direct formic acid fuel cells, Journal of Power Sources 111 (2002) 83–89.
[13] Z.L. Liu, L. Hong, M.P. Tham, T.H. Lim, H.X. Jiang, Nanostructured Pt/C and Pd/C catalysts for direct formic acid fuel cells, Journal of Power Sources 161 (2006) 831–835.
[14] W.J. Zhou, J.Y. Lee, Particle size effects in Pd-catalyzed electrooxidation of formic acid, J Phys Chem C 112 (2008) 3789–3793.
[15] W.P. Zhou, A. Lewera, R. Larsen, R.I. Masel, P.S. Bagus, A. Wieckowski, Size effects in electronic and catalytic properties of unsupported palladium nanoparticles in electrooxidation of formic acid, J Phys Chem B 110 (2006) 13393–13398.
[16] M.H. Shao, K. Sasaki, R.R. Adzic, Pd-Fe nanoparticles as electrocatalysts for oxygen reduction, Journal of the American Chemical Society 128 (2006) 3526–3527.
[17] D.L. Wang, H.L. Xin, H.S. Wang, Y.C. Yu, E. Rus, D.A. Muller, F.J. DiSalvo, H.D. Abruna, Facile Synthesis of Carbon-Supported Pd-Co Core-Shell Nanoparticles as Oxygen Reduction Electrocatalysts and Their Enhanced Activity and Stability with Monolayer Pt Decoration, Chemistry of Materials 24 (2012) 2274–2281.
[18] C.Y. Du, M. Chen, W.G. Wang, G.P. Yin, Nanoporous PdNi Alloy Nanowires As Highly Active Catalysts for the Electro-Oxidation of Formic Acid, Acs Appl Mater Inter 3 (2011) 105–109.
[19] Q. Gao, Y.M. Ju, D. An, M.R. Gao, C.H. Cui, J.W. Liu, H.P. Cong, S.H. Yu, Shape-Controlled Synthesis of Monodisperse PdCu Nanocubes and Their Electrocatalytic Properties, Chemsuschem 6 (2013) 1878–1882.
[20] J.S. Jirkovsky, I. Panas, E. Ahlberg, M. Halasa, S. Romani, D.J. Schiffrin, Single Atom Hot-Spots at Au-Pd Nanoalloys for Electrocatalytic H2O2 Production, Journal of the American Chemical Society 133 (2011) 19432–19441.
[21] F. Gao, D.W. Goodman, Pd-Au bimetallic catalysts: understanding alloy effects from planar models and (supported) nanoparticles, Chemical Society Reviews 41 (2012) 8009–8020.
[22] S. Zhang, O. Metin, D. Su, S.H. Sun, Monodisperse AgPd Alloy Nanoparticles and Their Superior Catalysis for the Dehydrogenation of Formic Acid, Angew Chem Int Edit 52 (2013) 3681–3684.
[23] H. Zhang, M.S. Jin, H.Y. Liu, J.G. Wang, M.J. Kim, D.R. Yang, Z.X. Xie, J.Y. Liu, Y.N. Xia, Facile Synthesis of Pd-Pt Alloy Nanocages and Their Enhanced Performance for Preferential Oxidation of CO in Excess Hydrogen, Acs Nano 5 (2011) 8212–8222.
[24] Z.N. Zhu, H.F. Meng, W.J. Liu, X.F. Liu, J.X. Gong, X.H. Qiu, L. Jiang, D. Wang, Z.Y. Tang, Superstructures and SERS Properties of Gold Nanocrystals with Different Shapes, Angew Chem Int Edit 50 (2011) 1593–1596.
[25] H.C. Lee, Y. Potapova, D. Lee, A core-shell structured, metal-ceramic composite-supported Ru catalyst for methane steam reforming, Journal of Power Sources 216 (2012) 256–260.
[26] E. McFarland, Unconventional Chemistry for Unconventional Natural Gas, Science 338 (2012) 340–342.
[27] M. Wakisaka, S. Mitsui, Y. Hirose, K. Kawashima, H. Uchida, M. Watanabe, Electronic structures of Pt-Co and Pt-Ru alloys for Co-tolerant anode catalysts in polymer electrolyte fuel cells studied by EC-XPS, J Phys Chem B 110 (2006) 23489–23496.
[28] H. Ataee-Esfahani, J. Liu, M. Hu, N. Miyamoto, S. Tominaka, K.C.W. Wu, Y. Yamauchi, Mesoporous Metallic Cells: Design of Uniformly Sized Hollow Mesoporous PtRu Particles with Tunable Shell Thicknesses, Small 9 (2013) 1047–1051.
[29] D. Wu, M. Cao, M. Shen, R. Cao, Sub-5 nm Pd–Ru Nanoparticle Alloys as Efficient Catalysts for Formic Acid Electrooxidation, Chemcatchem 6 (2014) 1731–1736.
[30] D.S. Wu, Z.L. Zheng, S.Y. Gao, M.N. Cao, R. Cao, Mixed-phase PdRu bimetallic structures with high activity and stability for formic acid electrooxidation, Phys Chem Chem Phys 14 (2012) 8051–8057.
[31] K. Kusada, H. Kobayashi, R. Ikeda, Y. Kubota, M. Takata, S. Toh, T. Yamamoto, S. Matsumura, N. Sumi, K. Sato, K. Nagaoka, H. Kitagawa, Solid Solution Alloy Nanoparticles of Immiscible Pd and Ru Elements Neighboring on Rh: Changeover of the Thermodynamic Behavior for Hydrogen Storage and Enhanced CO-Oxidizing Ability, Journal of the American Chemical Society 136 (2014) 1864–1871.
[32] T.R. Garrick, W.J. Diao, J.M. Tengco, E.A. Stach, S.D. Senanayake, D.A. Chen, J.R. Monnier, J.W. Weidner, The Effect of the Surface Composition of Ru-Pt Bimetallic Catalysts for Methanol Oxidation, Electrochimica Acta 195 (2016) 106–111.
[33] M. Wojdyr, Fityk: a general-purpose peak fitting program, J Appl Crystallogr 43 (2010) 1126–1128.
[34] Y. Luo, L. Calvillo, C. Daiguebonne, M.K. Daletou, G. Granozzi, N. Alonso-Vante, A highly efficient and stable oxygen reduction reaction on Pt/CeOx/C electrocatalyst obtained via a sacrificial precursor based on a metal-organic framework, Appl Catal B-Environ 189 (2016) 39–50.
[35] Y. Luo, N. Shroti, M.K. Daletou, L.A. Estudillo-Wong, N. Alonso-Vante, Synergistic effect of Yttrium and pyridine-functionalized carbon nanotube on platinum nanoparticles toward the oxygen reduction reaction in acid medium, J Catal 344 (2016) 712–721.
[36] S. Sandlobes, M. Friak, S. Zaefferer, A. Dick, S. Yi, D. Letzig, Z. Pei, L.F. Zhu, J. Neugebauer, D. Raabe, The relation between ductility and stacking fault energies in Mg and Mg-Y alloys, Acta Mater 60 (2012) 3011–3021.
[37] Y.H. Zhao, X.Z. Liao, Y.T. Zhu, Z. Horita, T.G. Langdon, Influence of stacking fault energy on nanostructure formation under high pressure torsion, Mat Sci Eng a-Struct 410 (2005) 188–193.
[38] J.W. Wang, S. Narayanan, J.Y. Huang, Z. Zhang, T. Zhu, S.X. Mao, Atomic-scale dynamic process of deformation-induced stacking fault tetrahedra in gold nanocrystals, Nat Commun 4 (2013).
[39] N. Hoshi, K. Kagaya, Y. Hori, Voltammograms of the single-crystal electrodes of palladium in aqueous sulfuric acid electrolyte: Pd(S)-[n(111) × (111)] and Pd(S)-[n(100) × (111)], Journal of Electroanalytical Chemistry 485 (2000) 55–60.
[40] H. Duncan, A. Lasia, Separation of hydrogen adsorption and absorption on Pd thin films, Electrochimica Acta 53 (2008) 6845–6850.
[41] N. Cheng, H. Lv, W. Wang, S. Mu, M. Pan, F. Marken, An ambient aqueous synthesis for highly dispersed and active Pd/C catalyst for formic acid electro-oxidation, Journal of Power Sources 195 (2010) 7246–7249.
[42] D.A.J. Rand, R. Woods, The nature of adsorbed oxygen on rhodium, palladium and gold electrodes, Journal of Electroanalytical Chemistry 31 (1971) 29–38.
[43] Z.Y. Zhou, X.W. Kang, Y. Song, S.W. Chen, Butylphenyl-functionalized palladium nanoparticles as effective catalysts for the electrooxidation of formic acid, Chem Commun 47 (2011) 6075–6077.
[44] J. Bao, M. Dou, H. Liu, F. Wang, J. Liu, Z. Li, J. Ji, Composition-dependent electrocatalytic activity of palladium-iridium binary alloy nanoparticles supported on the multiwalled carbon nanotubes for the electro-oxidation of formic acid, Acs Appl Mater Inter 7 (2015) 15223.
[45] Z. Liu, X. Zhang, S.W. Tay, Nanostructured PdRu/C catalysts for formic acid oxidation, Journal of Solid State Electrochemistry 16 (2012) 545–550.
[46] Y.Z. Lu, W. Chen, One-pot synthesis of heterostructured Pt-Ru nanocrystals for catalytic formic acid oxidation, Chem Commun 47 (2011) 2541–2543.